Nanospectroscopy of Infrared Phonon Resonance Enables Local Quantification of Electronic Properties in Doped SrTiO$_3$ Ceramics

Martin Lewin, Christoph Baeumer, Felix Gunkel, Alexander Schwedt, Fabian Gaussmann, Jochen Wueppen, Paul Meuffels, Bernd Jungbluth, Joachim Mayer, Regina Dittmann, Rainer Waser, and Thomas Taubner*

Among the novel materials for electronic applications and novel device concepts beyond classical Si-based CMOS technology, SrTiO$_3$ represents a prototype role model for functional oxide materials: It enables resistive switching, but can also form a 2D electron gas at its interface and thus enables tunable transistors. However, the interplay between charge carriers and defects in SrTiO$_3$ is still under debate. Infrared spectroscopy offers the possibility to characterize structural and electronic properties of SrTiO$_3$ in operando, but is hampered by the diffraction-limited resolution. To overcome this limitation and obtain nanoscale IR spectra of donor-doped Sr$_{1-x}$La$_x$TiO$_3$ ceramics, scattering-type scanning near-field optical microscopy is applied. By exploiting plasmon–phonon coupling, the local electronic properties of doped SrTiO$_3$ are quantified from a detailed spectroscopic analysis in the spectral range of the near-field 'phonon resonance'. Single crystal-like mobility, an increase in charge carrier density N and an increase in ε_∞ at grain boundaries ($\mu \approx 5.7$ cm^2 V^{-1}s^{-1}, $N = 7.1 \times 10^{19}$ cm^{-3}, and $\varepsilon_\infty = 7.7$) and local defects ($\mu \approx 5.4$ cm^2 V^{-1}s^{-1}, $N = 1.3 \times 10^{20}$ cm^{-3}, and $\varepsilon_\infty = 8.8$) are found. In future, subsurface quantification of defects and free charge carriers at interfaces and filaments in SrTiO$_3$ can be envisioned.

1. Introduction

In order to overcome the limits of classical Si based CMOS technology in the future, intensive research on novel materials and emerging devices is driving research and development in industry and academia.[1] The unique electronic properties of complex oxides, such as superconductivity, ferroelectricity, magnetoresistivity, and non-volatile resistive switching, enable novel multi-functional devices, which cannot be realized using conventional Si technology.[2,3] SrTiO$_3$ is a prototype role model for functional oxides and in its pristine form a bulk insulator. At its surface and at heterointerfaces such as LaAlO$_3$–SrTiO$_3$ highly conductive 2D electron gases (2DEG) can be observed.[4,5] Based on this unique functionality, novel ultra-confined electronic devices can be envisioned, while monolithic integrated circuits[6] and transistors with an on-off ratio of up to 10^6 are already demonstrated.[7] However, the formation mechanism of the 2D interface states and especially the interaction of structural and electronic properties is still under debate.[8,9] Due to its well-known defect chemistry SrTiO$_3$ serves as a model system for redox-based resistive random access memory (ReRAM).[1,10,11] Here, the resistance of SrTiO$_3$ devices is switched electronically in a reversible and non-volatile manner, based on the migration of oxygen vacancies, which act as donor dopants.[10] Also for ReRAM applications, defects play a crucial role. Even the resistive switching process itself is considered to essentially rely on local defects.[12–14] Spatially unresolved integral measurements are not sufficient to

M. Lewin, Prof. T. Taubner
Institute of Physics (IA)
RWTH Aachen University
52065 Aachen, Germany
E-mail: taubner@physik.rwth-aachen.de

The ORCID identification number(s) for the author(s) of this article can be found under https://doi.org/10.1002/adfm.201802834.

Dr. C. Baeumer, Dr. P. Meuffels, Prof. R. Dittmann
Peter Grünberg Institute
Forschungszentrum Juelich
52425 Juelich, Germany

Dr. A. Schwedt, Prof. J. Mayer
Central Facility for Electron Microscopy
RWTH Aachen University
52065 Aachen, Germany

Dr. F. Gaussmann, Dr. J. Wueppen, Dr. B. Jungbluth
Fraunhofer Institute for Laser Technology (ILT)
Steinbachstr. 15, 52074 Aachen, Germany

Dr. F. Gunkel, Prof. R. Waser
Institute of Electronic Materials (IWE2)
RWTH Aachen University
52065 Aachen, Germany

understand the interplay of structural and electronic properties in SrTiO₃. Hence, new non-destructive and subsurface-sensitive methods have to be applied to investigate oxide surfaces, interfaces and devices on the nanometre (nm) scale.

Recently, the in-operando subsurface investigation of memristive devices was enabled by X-ray photoemission electron microscopy (XPEEM) by employing a graphene top electrode.[15] The formation of a conductive filament was imaged directly by analyzing the valence state of Ti. However, no structural information was obtained and the analysis was limited by the probing depth (several nm) and the availability of a synchrotron source. Both local conducting atomic force microscopy[12] and impedance spectroscopy can yield valuable information about the electronic properties, but no structural information. So far only transmission electron microscopy (TEM) has proven to yield structural information about grain boundaries in SrTiO₃ in combination with maps of the electron density by electron holography.[16] However, multiple assumptions about the local potential distributions have to be made and the investigation is usually limited to the post-mortem analysis of electron-transparent membrane or lamella samples with a thickness of only several tens of nm. Optical methods promise to be much easier to handle (a direct comparison of the different techniques is summarized in Table S1, Supporting Information). By nature, infrared spectroscopy and even Raman spectroscopy are sensitive to structural properties and electronic properties of SrTiO₃ in parallel. Recently, fluorescence life time imaging and confocal Raman microscopy were successfully applied to image inhomogeneities in SrTiO₃ single crystals.[17,18] Especially, the infrared far-field reflectivity of SrTiO₃ crystals was extensively studied in the nominally undoped case,[19] for different doping levels,[20] reducing conditions[21] and temperature ranges.[22,23] However, due to the diffraction limit no information on the nm scale could be resolved. We overcome this limitation by applying scattering-type scanning near-field optical microscopy (s-SNOM) to obtain infrared near-field spectra of SrTiO₃ with a wavelength independent spatial resolution of 25 nm.[24] Using this approach, a metal-coated AFM tip, which is irradiated by an infrared light source, confines the near-field interaction of tip and sample to the nm scale by the small size of the tip apex. Local spectral information can be obtained by interferometrically analyzing the back scattered light and sequentially scanning the tip relative to the sample at different wavelengths of a high-irradiance single-wavelength source. Alternatively, a broad-band light source is applied to obtain near-field spectra at each tip position by scanning a reference mirror like in conventional Fourier transform infrared spectroscopy (nano-FTIR).[25–27]

The near-field interaction of tip and sample depends on the local permittivity $\varepsilon_s(v)$ of the sample. The amplitude of the scattered field $s(v)$ from the coupled system exhibits a resonance peak near v_{res} for $\mathrm{Re}[\varepsilon_s(v_{res})] \approx -3, ..., -1$ (assuming low losses, small $\mathrm{Im}[\varepsilon_s(v_{res})]$).[24] Near-field resonances can be observed for various polaritonic materials, showing a negative permittivity: The so called 'phonon resonance' of lattice vibrations near v_{LO}[28] or the so-called 'plasmon resonance' near the plasma frequency v_p of free charge carriers.[29,30] The quantitative interaction of tip and sample can be modeled quite accurately by a dipolar near-field interaction of charges in the tip with image charges in the sample.[31] This gave rise to the quantification of structural

defects in the wide bandgap materials GaN[32] and SiC,[33] as well as free charge carrier profiling in semiconductor nanostructures.[34–37] The plasma frequency depends on the doping concentration and lies for SrTiO₃ usually in the terahertz spectral range at very low frequencies due to a very high effective mass ($m_{eff} \approx 6.5\ m_e$).[38] Hence, the usual approach to quantify the electronic properties by performing spectroscopy at the near-field 'plasmon resonance' is limited by the availability of beamline facilities offering a tunable/broad-band terahertz light source (synchrotron, free electron laser, etc.). However, both phonon and charge carrier contributions can interact, which leads to coupled plasmon–phonon modes.[39,40] Huber *et al.* demonstrated that the phonon near-field resonance of SiC is also sensitive to electronic variations.[41] Very recently, first reports of recorded near-field spectra of the SrTiO₃ phonon resonance were published, however any quantitative characterization, especially of the free charge carrier influence, is still missing.[42,43] We now demonstrate by exploiting plasmon–phonon coupling that s-SNOM can be used to extract the electronic properties at SrTiO₃ interfaces on the nm scale with a table-top setup.

2. Influence of Free Charge Carriers on Phonon Resonance

To demonstrate the interplay of structural defects and free charge carriers, we investigated polycrystalline Sr₁₋ₓLaₓTiO₃ ceramics containing a large number of grain boundaries. Those ceramics were moderately donor doped with a concentration of 0.30 atomic percent of lanthanum. Since the ceramics have been processed at moderate reducing conditions, we can assume the ceramics are in the electron doped regime where the carrier concentration is fixed by the donor concentration ($N \approx 5 \times 10^{19}\ \mathrm{cm}^{-3}$).[44] To detect even small electronic variations in the polycrystalline system, we first estimate the influence of free charge carriers on the strong near-field signal at the phonon resonance v_{LO}. Therefore, we use a simplified model with a limited number of parameters to describe the permittivity $\varepsilon(v) = \varepsilon'(v) + i\varepsilon''(v)$ of SrTiO₃, which allows for a clear physical interpretation.[19,39] To a first degree the influence of free carriers on the optical permittivity can be described by a simple superposition of three phonons and the free electron contributions:[39]

$$\varepsilon(v) = \varepsilon_\infty + \sum_j^3 4\pi\rho_j \frac{v_j^2}{v_j^2 - v^2 - iv\gamma_j} - \frac{v_p(N)^2}{v^2 + iv\Gamma_{\mathrm{Drude}}};\quad v_p(N) = \frac{1}{2\pi c_0}\sqrt{\frac{Ne^2}{\varepsilon_0 m_{eff}}} \quad (1)$$

Here, ε_∞ summarizes contributions from higher frequencies, ρ_j describes the strength, and γ_j the width of each phonon resonance, while their position is given by the resonance frequencies v_j. The free electrons are characterized by the plasma frequency v_p, which is given by the effective mass m_{eff} and the charge carrier density N, and by the electronic damping constant Γ_{Drude}. The damping constant can be converted to the scattering time $\tau = \dfrac{1}{2\pi c_0 \Gamma_{\mathrm{Drude}}}$ and is directly linked to the mobility $\mu = \dfrac{e\tau}{m_{eff}}$ of the charge carriers. Literature data for all the parameters are collected in Table S2 (Supporting Information). More elaborate models take into account polaron effects at high frequencies,[39,45] frequency-dependent damping constants
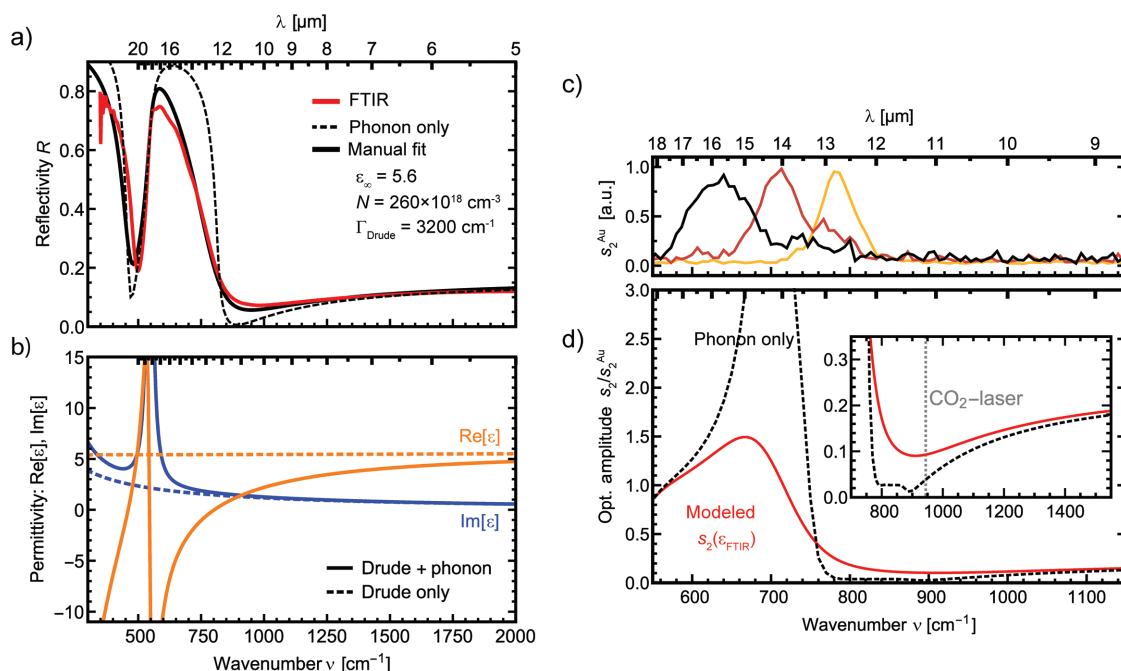
Figure 1. Far-field characterization to estimate the free charge carrier influence on the phonon near-field resonance of $SrTiO_3$: a) an FTIR reflectivity spectrum of the doped $Sr_{0.997}La_{0.003}TiO_3$ ceramic (red solid line) was used to derive its electronic properties according to Equation (1) from a manual fit of the reflectivity $R(\varepsilon_{FTIR}(\nu))$ (black solid line). For comparison, the expected reflectivity spectrum without free charge carriers is shown (black dashed line). The corresponding real (orange) and imaginary parts (blue) of the dielectric function $\varepsilon_{FTIR}(\nu)$ (solid lines) are given in (b). Additionally, the dielectric contribution of the charge carriers only is shown (dashed lines). The dielectric function $\varepsilon_{FTIR}(\nu)$ was subsequently used in combination with the finite dipole model[31] to calculate the expected near-field amplitude spectrum $s_2[\varepsilon(\nu)]/s_2^{Au}$ (red solid line) in d). In comparison, the expected near-field spectrum of nominally undoped $SrTiO_3$ is shown (black dashed line). A zoom-in is shown in the inset and the wavenumber of the CO_2 laser $\nu = 944$ cm^{-1} for monochromatic imaging outside the phonon resonance is marked. The spectrum of the broad-band laser system for three different central wavelengths is sufficient to cover the phonon resonance of $SrTiO_3$ as can be seen in (c). The near-field spectra of the laser were obtained on a 30 nm thick Au-film and normalized to the maximum value.

or different damping constants for TO and LO phonons.[23] However, the simple superposition of electronic and phononic contributions was found to yield a reasonable and physically insightful explanation of the experimental observations.

As a starting point for the near-field analysis, we recorded a spatially unresolved far-field infrared reflectivity spectrum of nearly the whole ceramic (aperture ≈ several mm) using a standard FTIR (see **Figure 1**a, red solid line). Additionally, the reflectivity $R(\varepsilon(\nu))$ was calculated from the dielectric function in Equation (1) for the case of an undoped single crystal ($N < 1 \times 10^{18}$ cm^{-3}, black dashed line) and by manually adjusting ε_∞, N, and Γ_{Drude} to the best fit (black solid line) with the experimental spectrum. Clearly, the FTIR spectrum of the doped ceramic shows a reduced reflectivity and a narrowing of the Restrahlen band between 12 and 18 µm compared to the phonon resonance of the undoped $SrTiO_3$ crystal in literature. Qualitatively, the experimental data can be reproduced by the fitted reflectivity spectrum for a free charge carrier density of $N = 26 \times 10^{19}$ cm^{-3} at a high damping rate of $\Gamma_{Drude} = 3200$ cm^{-1} ($\mu = 0.5$ cm^2 V^{-1}s^{-1}). Below the corresponding dielectric function of the fit $\varepsilon_{FTIR}(\nu)$ is shown in Figure 1b. Due to the nearly constant real part of the dielectric function no significant shift of the phonon resonance is observed. At the same time, the additional imaginary part of the dielectric function due to the charge carriers causes the reduced reflectivity and the narrowing of the Reststrahlen band. The quantitative deviations between the fit

and the experimental far-field reflectivity spectrum already indicate a spatially inhomogeneous infrared response.

To obtain quantitative information about local variations of the charge carriers and phonons, we use infrared s-SNOM to circumvent the diffraction limit and gain the same information as in FTIR, however at a spatial resolution of 25 nm. Commercially available tunable gas lasers and quantum cascade lasers yield a sufficient signal strength for monochromatic imaging in the range between $\lambda = 5$ and 12 µm. However, light sources covering the spectral range between $\lambda = 12$ and 18 µm, which are applicable to s-SNOM, are rarely found. In general, synchrotron radiation,[46,47] free electron lasers,[48] thermal sources[25,49] or super-continuum laser sources[26,50,51] are used. The practical limitations of large beamline facilities (synchrotron sources and free electron lasers) and the low signal-to-noise ratio of thermal sources motivated the development of our home-built tabletop broad-band-laser system (see Experimental Section)[32,52] Our setup is, in contrast to other super-continuum laser sources, especially designed for the long-wavelength regime up to $\lambda = 18$ µm. Due to its narrow bandwidth of ≈100 cm^{-1}, it yields a much better signal-to-noise ratio at mW power levels compared to other super-continuum laser sources, enabling to address the phonon frequencies of wide bandgap semiconductors (e.g., GaN, SiC, TiO_2, and $SrTiO_3$). The spectral range of our broad-band laser source is shown in Figure 1c. By tuning the central emission wavelength to three different positions, we can cover

1802834 (3 of 11)

**ADVANCED
SCIENCE NEWS**

www.advancedsciencenews.com

**ADVANCED
FUNCTIONAL
MATERIALS**

www.afm-journal.de

the full range of the expected near-field phonon resonance of SrTiO$_3$, which is depicted below in Figure 1d. The near-field optical amplitude spectra $s_2[\varepsilon(\nu)]/s_2^{Au}$ are calculated from the dielectric function in Equation (1) using the Finite Dipole Model[31] for two different configurations: only the phonon resonance of nominally undoped crystalline SrTiO$_3$ (charge carrier density $N < 1 \times 10^{18}$ cm^{-3}, black dashed line) and for a combination of phonon and charge carrier contributions using the far-field fitted dielectric function of the doped ceramic $\varepsilon_{FTIR}(\nu)$ (red solid line). In both cases, a resonance peak of the near-field amplitude is expected. The additional damping of the charge carriers reduces the height and shifts the phonon resonance to slightly lower wavenumbers. However, for all wavenumbers $\nu > 760$ cm^{-1}, the near-field amplitude signal with additional charge carriers is expected to be higher compared to the nominally undoped case (phonon only, cf. inset of Figure 1d). This corresponds to an inversion of the signal contrast of charge carrier-rich and charge carrier-poor regions of SrTiO$_3$ near $\nu = 760$ cm^{-1}. Hence, to visualize and identify regions of different electronic properties we use monochromatic imaging above the phonon near-field resonance at $\nu = \lambda^{-1} = (10.6 \ \mu m)^{-1} = 944$ cm^{-1} (gray line in inset of Figure 1d). In contrast to hyperspectral imaging[27] (obtaining spectra at each pixel using nano-FTIR), the higher signal-to-noise ratio of a continuous-wave CO$_2$ laser can be used to identify even subtle relative changes in a large area.

3. Identification of Grain Boundaries by Monochromatic Imaging

A near-field optical amplitude image $s_2[\varepsilon(\nu)]/s_2^{Au}$ of the Sr$_{0.997}$La$_{0.003}$TiO$_3$ ceramic at $\nu = 944$ cm^{-1} is depicted in **Figure 2**a. Strong inhomogeneities in the infrared response on the nm scale can be identified in this off-resonant image. These features do not stem from topographic artifacts as no equivalent pattern can be found in the corresponding topography image (see Figure S1, Supporting Information). Strikingly, a mosaic pattern with enhanced near-field amplitude can be identified (marked by a white 'G'). The center of the mosaics often appears dark and shows a low off-resonant near-field amplitude (marked by a white 'D'). Bright circular spots (marked by a white 'B') were found to yield the highest off-resonant near-field amplitude.

To verify the origin of the mosaics, electron backscatter diffraction (EBSD, see Experimental Section) maps of the local crystal orientation at each position were collected in the same region (see Figure 2b). In Figure 2c, the near-field optical amplitude image is superimposed with the EBSD map of the grain boundaries. Obviously, the mosaic shaped features ('G') of enhanced off-resonant near-field amplitude coincide with the grain boundaries. The dark regions ('D') of low near-field amplitude are found in the center of the grains, while the bright spots ('B') appear to be attached closely to the grain boundaries. Thus, we confirm that s-SNOM is sensitive to grain boundaries in SrTiO$_3$.

4. Spectroscopic Evaluation

The direct correlation of the EBSD maps and the s-SNOM images allows now for the first time to analyze infrared near-field
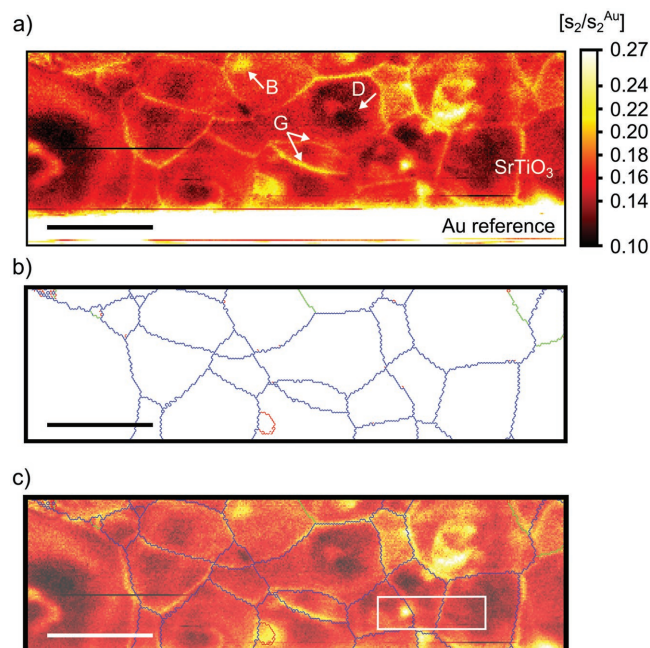

Figure 2. Correlative s-SNOM imaging and EBSD mapping of grain boundaries: a) near-field optical amplitude image s_2/s_2^{Au} of the doped Sr$_{0.997}$La$_{0.003}$TiO$_3$ ceramic taken at $\nu = 944$ cm^{-1}. The amplitude is normalized to the adjacent gold film, which was deposited lithographically. Mainly two types of inhomogeneities with an enhanced near-field amplitude outside the phonon resonance can be found: circular spots (marked with a white 'B') and mosaic-shaped features (marked with a white 'G'). Furthermore, dark regions with a low near-field amplitude (marked with a white 'D') can be observed. b) EBSD map of the grain boundaries in the same region with the color-coded angular misorientation: (1°-5° red, 5°–15° green, >15° blue). c) Superposition of SrTiO$_3$ region in (a) and (b). White rectangle indicates position of high-resolution zoom-in image shown in Figure 3. Scale bar in all images: 2 µm.

amplitude spectra of SrTiO$_3$ from a single grain boundary. Near-field amplitude spectra were acquired from three different positions, as marked in the high-resolution near-field optical amplitude image in **Figure 3**a. The corresponding near-field amplitude spectra s_2/s_2^{Au} are depicted in Figure 3b. Additionally, the calculated near-field spectra from Figure 1d for an undoped SrTiO$_3$ crystal and the near-field resonance, which was derived from the far-field spectrum of the doped ceramic, are included. All three spectra show a near-field resonance centered at about 660–670 cm^{-1}, which corresponds to a significant shift compared to the near-field phonon resonance of an undoped single crystal. While the center of the grains ('D') shows a strong phonon resonance, the peak heights at the bright circular spot ('B') and at the grain boundary ('G') are much lower. In contrast for wavenumbers $\nu > 720$ cm^{-1}, the near-field amplitude is always higher at the bright circular spot ('B') compared to the other spots. This contrast inversion, which leads to a deviation of the spectra from each other and from the undoped single crystal on a broad spectral range, clearly reveals inhomogeneities of the electronic properties of the ceramic. If mainly a change of the phononic contributions was the cause, also a relative wavenumber shift of the phonon resonance should be observable. While the near-field spectra at the bright spot ('B') appear to agree with the interpretation of low mobile charge carriers, as derived from the
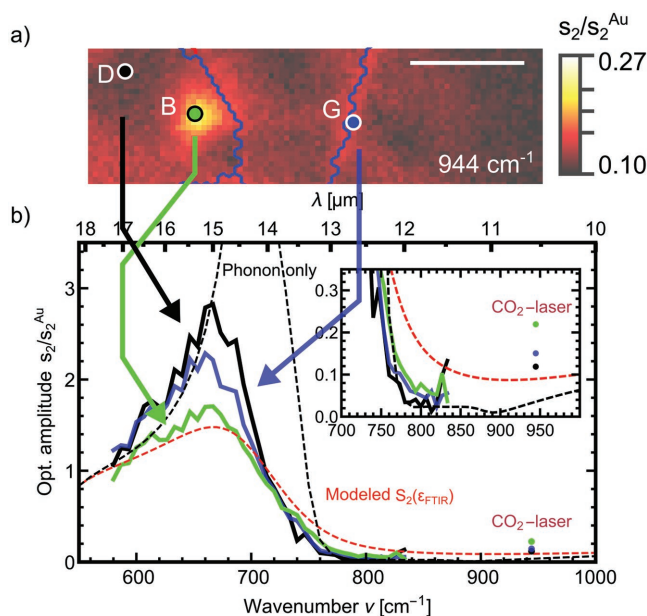
Figure 3. Obtaining nano-FTIR spectra of single defect and grain boundary: a) high-resolution near-field optical amplitude image taken at $v = 944\ cm^{-1}$ with grain boundaries indicated in blue. Scale bar: 500 nm. b) Near-field optical amplitude spectra taken at three different positions in (a): in the center of a grain ('D', black line), on a circular spot ('B', green line), on a single grain boundary ('G', blue line). The contrasts obtained from monochromatic imaging are marked by single dots. For comparison, the calculated contrasts from Figure 1d for the phonon resonance of an undoped single crystal and the expected contrast from the bulk far-field FTIR spectra of the whole ceramic are included.

far-field FTIR spectrum, significant differences for wavenumbers above the phonon resonance can be found (inset in Figure 3b): at $v = 800\ cm^{-1}$, a minimum of the near-field amplitude s_2 with almost zero amplitude is measured, but the model predicts a finite amplitude. Additionally, the signal amplitude is found to increase for $v > 820\ cm^{-1}$ and the observed near-field amplitude with the CO_2 laser at $v = 944\ cm^{-1}$ is much higher than predicted. In fact, a high imaginary part of the permittivity $Im[\varepsilon]$ due to low-mobile charge carriers would always cause a finite, nearly constant signal in the anti-resonance near $v = 800\ cm^{-1}$ and cannot explain the strong increase in near-field amplitude for wavenumbers $v > 820\ cm^{-1}$. As a consequence, to quantify the electronic properties, also the high-frequency range has to be evaluated spectroscopically.

The region of interest from Figures 2 and 3 was contaminated with carbon after the EBSD mapping and any plasma cleaning might have changed the electronic properties. Therefore, we searched for a comparable region on the same ceramic, with a similar near-field contrast at $v = 944\ cm^{-1}$. In **Figure 4**, this comparable region was investigated by performing sequential spectroscopy from $v = 871$ to $1510\ cm^{-1}$. In Figure 4a, the optical amplitude image taken with a quantum cascade laser at a wavenumber of $v = 944\ cm^{-1}$ is shown. The same features as in Figure 2 can be identified at a similar near-field optical amplitude (same color code). Therefore, we combined the low- and high-frequency near-field spectra from both regions into one broad-band near-field optical amplitude spectrum in Figure 4b. The high-frequency data points, which were obtained by
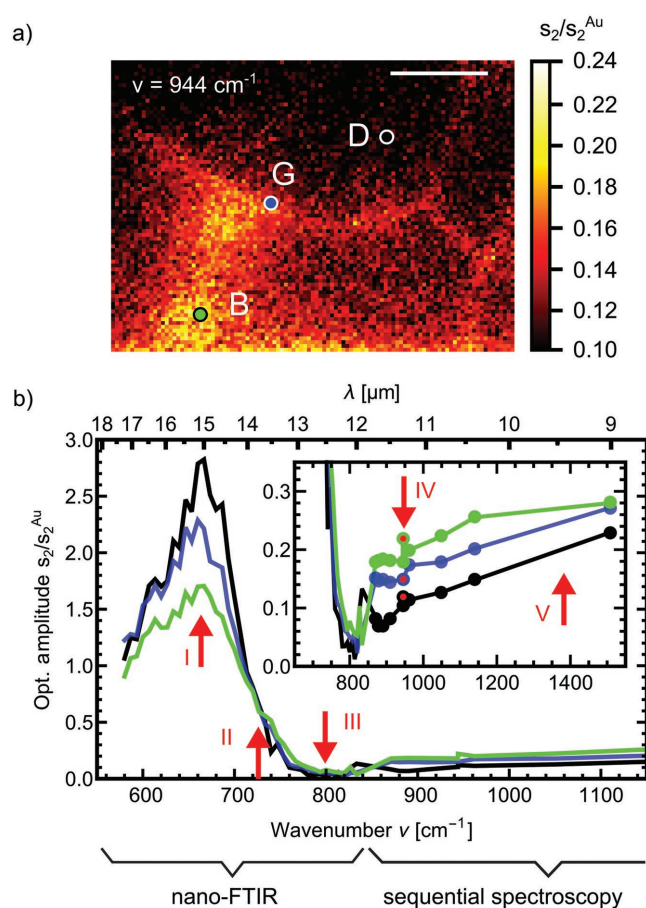

Figure 4. Sequential spectroscopy to probe high-frequency contributions in a comparable region: a) near-field optical amplitude image s_2/s_2^{Au} of a region, which is comparable to the one in Figure 3a. Image taken at $v = 944\ cm^{-1}$. The same color coding as in Figure 3a was used: center of a grain ('D', black), circular spots ('B', green), and grain boundary ('G', blue). Scale bar: 500 nm. b) Combined spectroscopic data of nano-FTIR point spectra from Figure 3 and sequential spectroscopic data points (marked with circular dots) collected in the comparable region in (a). Five characteristic points are marked. I: phonon resonance at $v = 660\ cm^{-1}$, II: contrast inversion at $v = 720\ cm^{-1}$, III: anti-resonance at $v = 800\ cm^{-1}$, IV: off-resonant contrast using a CO_2 laser at $v = 944\ cm^{-1}$ (red dots), and V: high-frequency contrast.

sequential spectroscopy, are additionally marked by circular dots in the inset. Five characteristic points can be found in Figure 4b, which need to be explained: (I) the damping of the phonon resonance at $v = 660\ cm^{-1}$ without any significant wavenumber shift, (II) the contrast inversion at $v = 720\ cm^{-1}$, (III) the anti-resonance at $v = 800\ cm^{-1}$, (IV) the off-resonant contrast using a CO_2 laser at $v = 944\ cm^{-1}$ (red dots), and (V) the high-frequency contrast. The high-frequency spectroscopic data show a nearly parallel vertical shift of the near-field optical amplitude signal level from 'D' to 'G' to 'B'. This is a clear indication that a local change of mobility and charge carrier density solely cannot explain the observed features or yield quantitatively correct values for N and Γ_{Drude}. Apparently, the dielectric function $\varepsilon(v)$ has to be adapted in the high-frequency range as a near-field optical contrast can be observed outside the resonance.

**ADVANCED
SCIENCE NEWS**

www.advancedsciencenews.com

**ADVANCED
FUNCTIONAL
MATERIALS**

www.afm-journal.de

5. Quantification of Charge Carrier Properties

To quantify the electronic properties, we have to separate the spectral influence of the charge carrier density N and the high-frequency offset ε_∞ on the phonon resonance. Therefore, the dielectric function $\varepsilon(\nu)$ and the corresponding near-field optical amplitude spectrum $s_2[\varepsilon(\nu)]/s_2^{Au}$ are calculated in **Figure 5** for three different combinations of ε_∞, N, and μ. In Figure 5a, ε_∞ is increased from 6.8 over 7.7 to 8.8 for an undoped single crystal of $SrTiO_3$. As ε_∞ is increased, the maximum amplitude of the phonon resonance is reduced and redshifted compared to the single crystal. In parallel, the signal amplitude at high frequencies above the phonon resonance is increased. In conclusion, it might explain the increase in the high-frequency signal amplitude observed in the experiment, but the spectral shift was much smaller. In the experiment, all the spectra showed a similar phonon resonance frequency (marked with a gray line in Figure 5).

An increase in highly mobile charge carriers ($\mu \sim \mu_{single\ crystal}$) in contrast to the strongly damped charge carriers in Figure 1 is modeled in Figure 5b. In this case, the change in the real and imaginary parts of the permittivity due to the increase of the plasma frequency ν_p causes a damping and a blueshift of the phonon near-field resonance. Albeit, the observed high-frequency contrast cannot be explained by an increase in the charge carrier density N. Only a combination of both effects can explain all of the five characteristic points observed experimentally. To yield quantitative values of the carrier properties, the high-frequency near-field amplitude signal was adjusted manually by varying ε_∞ to fit the experimental spectrum. Afterwards, the optimum values for N and Γ_{Drude} were derived from an automatic fit. The combined experimental near-field optical amplitude spectra and the fitted near-field spectrum are plotted in Figure 5d separately for the dark center of the grains ('D'), the grain boundary ('G'), and the bright circular spot ('B'). Clearly, the accordance of spectra and fit now allow
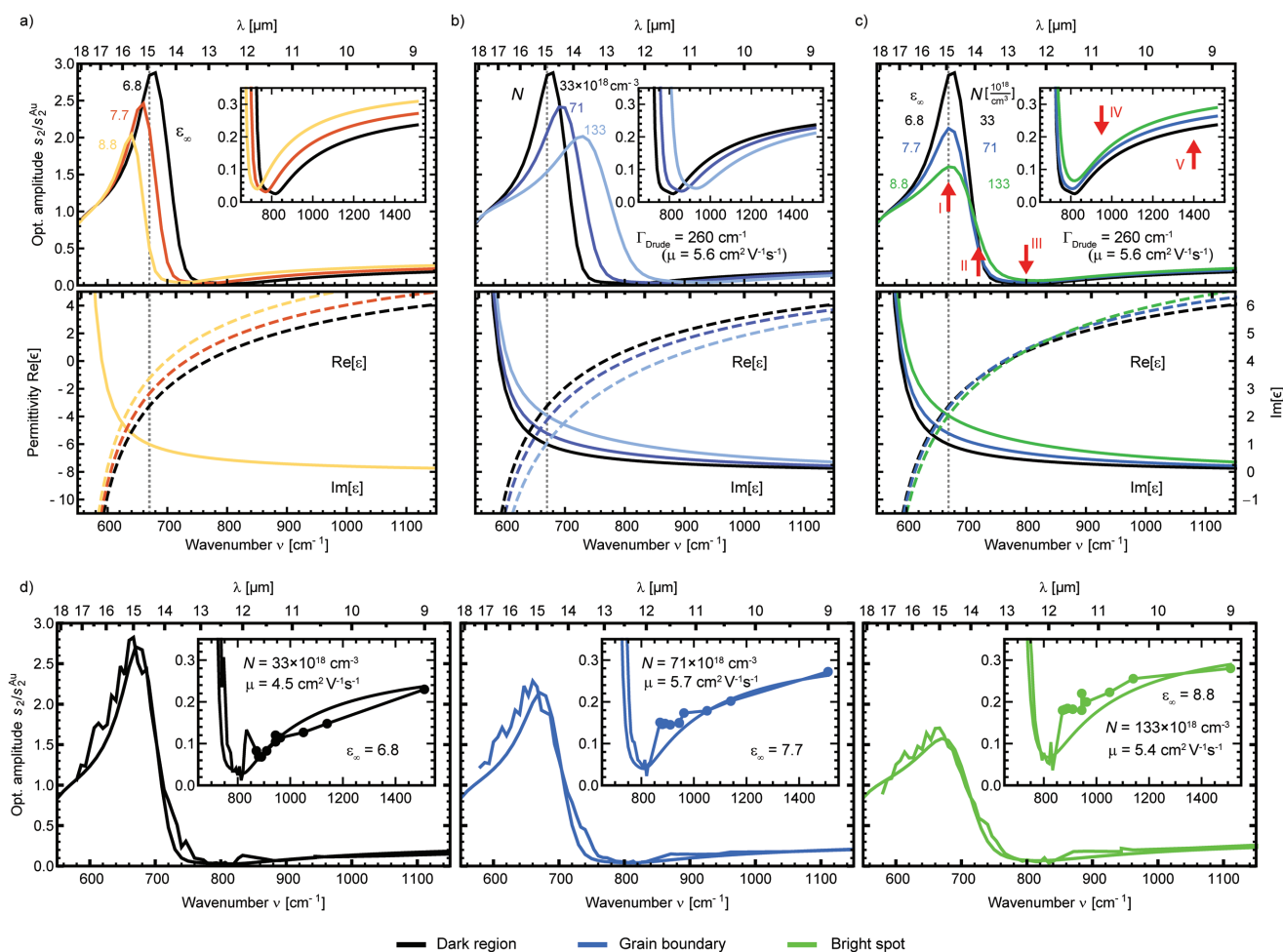

Figure 5. Shift of near-field resonance by increasing high-frequency offset ε_∞ and charge carrier density N: to separate the influences of ε_∞ and N on the phonon resonance, in (a), (b), and (c) near-field optical amplitude spectra $s_2[\varepsilon(\nu)]/s_2^{Au}$ (above) were calculated for three different variations of the dielectric function $\varepsilon(\nu)$ of $SrTiO_3$ (below) using the Finite Dipole Model. a) Increase only in the high-frequency offset of the dielectric function ε_∞ of an undoped crystal. b) Increase only in charge carrier density N at a constant low damping $\Gamma_{Drude} = 260\ cm^{-1}$ and a constant high-frequency offset $\varepsilon_\infty = 6.8$. c) Combination of both, an increase in charge carrier density N and an increase in the high-frequency offset ε_∞. In (a)–(c), the experimentally observed phonon resonance frequency is marked by a gray line. d) Fit of high-frequency offset ε_∞, charge carrier density N and charge carrier mobility μ to the combined near-field optical amplitude spectra from Figure 4b).

to locally derive the electronic properties of free charge carriers in $SrTiO_3$ from infrared near-field spectra: The charge carrier mobility μ appears to be relatively constant at the three points investigated and is only slightly lower than the mobility expected for doped $Sr_{0.997}La_{0.003}TiO_3$ single crystals at room temperature ($\mu \approx 7.5$ cm^2 V^{-1}s^{-1}).[44] The charge carrier concentration is found to be lowest at the center of the grain ('D', $N \approx 3.3 \times 10^{19}$ cm^{-3} and increases up to a value of $N \approx 1.3 \times 10^{20}$ cm^{-3} at the circular bright spot ('B'). At the grain boundary, a moderately increased charge carrier density of $N \approx 7.1 \times 10^{19}$ cm^{-3} is observed. In conclusion, the electronic conductivity $\sigma = Ne\mu$ is found to be higher at the grain boundary ('G', $\sigma_G \approx 66$ Ω^{-1} cm^{-1}) compared to the measurement inside the grain ('D', $\sigma_D \approx 24$ Ω^{-1} cm^{-1}), while the highest value is found in the circular spots ('B', $\sigma_B \approx 115$ Ω^{-1} cm^{-1}). Near-field optical imaging above the phonon resonance at, e.g., $\nu = 944$ cm^{-1} can therefore be used to detect highly conductive regions in $SrTiO_3$.

6. Discussion: Electron Accumulation at Interfaces in Donor-Doped $SrTiO_3$

The circular spots ('B') might result from dopant clustering as the carrier densities derived vary around the nominal bulk dopant concentration of the ceramic of $N \approx 5 \times 10^{19}$ cm^{-3}. Such an effect of dopant clustering has been already observed for Ba-doped $SrTiO_3$ nanoparticles.[53] For our case, it could be verified by future correlative elemental mapping (using, e.g., energy-dispersive X-ray-spectroscopy or atom probe tomography). A striking result of our study is the direct and locally resolved observation of electron accumulation at grain boundaries, particularly because we observe this effect in donor-doped $SrTiO_3$. Typically, in the literature, space charge layers at grain boundaries are characterized by spatially unresolved electrical characterization.[54] Furthermore, accumulation of electrons, accompanied with a depletion of electron holes, is typically reported only for acceptor-doped $SrTiO_3$. Spatially unresolved transport studies of acceptor doped $SrTiO_3$ ceramics reveal a strong reduction of the p-type charge carrier transport across the grain boundaries[54] and an increase in n-type transport along grain boundaries and surfaces[55] due to the formation of a negative space charge layer. These findings are supported by local impedance spectroscopy using microcontacts[56] and electron holography analysis.[16] The formation of the n-type space charge layer in all these acceptor-doped examples can be understood by the trapping of positively charged oxygen vacancies, which have a lower Gibbs energy at surfaces and interfaces as compared to the bulk.[55,57] Effectively, this results in a positive interface charge surrounded by a negatively charged electron accumulation layer. In contrast to that, and owing to its completely different defect chemistry,[58] donor-doped $SrTiO_3$ typically exhibits electron depletion layers at grain boundaries[44] and surfaces.[58–60] Interestingly, all these studies observe a blocking character of grain boundaries after treatments of donor-doped $SrTiO_3$ in oxidizing conditions. Under these oxidizing conditions, oxygen vacancies are effectively absent in donor-doped $SrTiO_3$, while Sr vacancy formation is the dominant defect formation process[58,61] (fundamentally different

from the acceptor-doped case discussed above). Accordingly, Moos and Härdtl explained the high resistance by negatively charged states at the grain boundaries (Sr vacancies), which cause the formation of 100 nm wide electron free depletion layers.[44] Only for donor-doped ceramics, which were reduced in water- and oxygen-free hydrogen atmospheres, a single crystal like behavior without any blocking influence from the grain boundaries was observed.[44] Additionally, Muenstermann et al. observed an enhanced transport in defect-rich regions in Nb-doped $SrTiO_3$ thin films.[62] In accordance with these results, our near-field analysis reveals not only the absence of electron blocking grain boundaries, but even more and for the first time enhanced electronic conductivity at the grain boundaries in donor-doped $SrTiO_3$.

We can reproduce this striking observation in a defect chemical model by taking into account the moderately reducing conditions of the ceramic preparation. Under these specific conditions, Sr vacancies potentially responsible for blocking grain boundaries are formed only in negligible concentration, while oxygen vacancies persist within the lattice (see Figure S2, Supporting Information, for calculations of defect concentrations formed during sample preparation). Hence, we propose: the low oxygen partial pressure during the final heat treatment in dry Ar/H$_2$ atmosphere (see Experimental Section) suppresses the formation of Sr vacancies,[58] while the trapping of oxygen vacancies at the interface causes an accumulation of negatively charged carriers surrounding the grain boundary. **Figure 6** displays the calculated charge carrier profiles for an accumulation of oxygen vacancies within the grain boundary core as obtained by self-consistently solving Poissons's equation and Gauss' law (see Ref. [58]). Given the nominal La doping of the ceramic, an oxygen vacancy concentration of 1.5×10^{20} cm^{-3} trapped in the grain boundary core is sufficient to increase the electron density in the vicinity of the grain boundary from $N \approx 5 \times 10^{19}$ cm^{-3} in the bulk to $N \approx 7.1 \times 10^{19}$ cm^{-3} at the grain boundary, thus, reproducing the experimental result obtained by the near-field analysis. The obtained core charge density is well comparable to reported values.[55,57] Our model calculations reveal an electron accumulation layer width of about 20–30 nm, slightly smaller
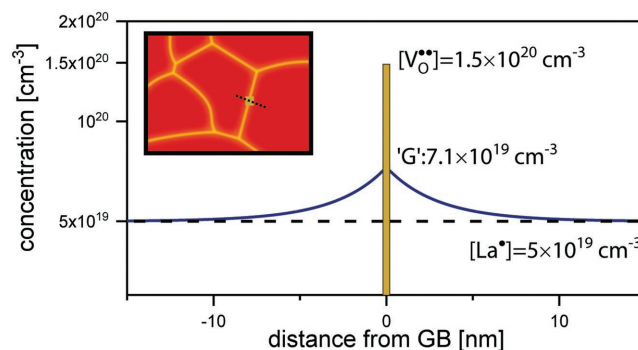

Figure 6. Model of n-type charge carrier accumulation at the grain boundaries. Calculated charge carrier profile across the grain boundary in La-doped $SrTiO_3$ (nominal doping level of $N \approx 5 \times 10^{19}$ cm^{-3}). Here, an accumulation of positively charged oxygen vacancies (1.5×10^{20} cm^{-3}) within the grain boundary core is assumed to reproduce the experimentally observed carrier density of $N \approx 7.1 \times 10^{19}$ cm^{-3}. In the inset, a sketch of the 2D charge carrier distribution is presented.

than the FWHM thickness of the grain boundary (≈100 nm) in the monochromatic s-SNOM images.

We have to note that s-SNOM is not sensitive to the sign of charges.[63] Only differences in the effective mass could be used to distinguish between them. However, the mobility values obtained from near-field analysis are extraordinarily consistent with values typically obtained from Hall measurements in $SrTiO_3$, which further confirms the validity of our model and identifies the probed carriers as electrons. The single crystal-like mobility observed in nano-FTIR spectra could result from a predominantly probed movement of charge carriers along the 3D grain boundaries and not across the grain boundary. The discrepancy between the results from the spatially unresolved far-field spectrum in Figure 1a and the near-field spectra might result from the strong inhomogeneities of the infrared response revealed on the nm scale and the different length scales of field confinement relative to the grain size ($d \approx 2$ μm). In addition, near-field spectra were only obtained from a small region of the mm-sized ceramic. Parallel to the charge carrier density N, the high-frequency offset of the dielectric function ε_∞ is found to increase from 6.8 to 8.8. To a small degree, this increase might stem from additional dopant atoms. However, in literature an additional mid-infrared absorption was reported for reduced $SrTiO_3$.[64] Just like for the ceramics in our case, the intensity of the absorption increased with increasing charge carrier density N, and was explained by intraband scattering processes.

7. Outlook: Identification of Locally Switched Conductive Spots Using Infrared s-SNOM

To give an outlook for ReRAM applications and to support our interpretation of the enhanced off-resonant signal to stem from higher electronic conductivity, we started to investigate the local resistive switching processes in a nominally undoped $SrTiO_3$ thin film. To this end, a 20 nm, pulsed-laser-deposited $SrTiO_3$ thin-film on a Nb-doped $SrTiO_3$ substrate was addressed electrically using a tungsten point probe (setup shown in **Figure 7**a), similar to Ref. [65]. A positive voltage ramp was applied to the probe while the Nb-doped $SrTiO_3$ substrate served as a grounded bottom electrode, resulting in the forming of a conductive filament with a resistance of 2 kΩ (voltage–current curve shown in Figure S3, Supporting Information). In a previous study, we found that similar conductive filaments in $SrTiO_3$ exhibit carrier densities in the range of $N \approx 1 \times 10^{21}$ cm^{-3}.[15] This range agrees very well with the electronic properties of the conductive regions revealed on the doped ceramics. Therefore, the same evaluation procedure, derived for the ceramic materials described above, can be applied to determine the properties of charge carriers due to oxygen vacancies in conductive filaments. In a second step, the switched conductive spot was imaged by monochromatic s-SNOM imaging above the phonon resonance at $v = 944$ cm^{-1} using a CO_2 laser. The near-field optical amplitude is shown in Figure 7b. Clearly, the switched conductive region shows a high off-resonant near-field amplitude. The absolute signal level and the relative signal contrast to the surrounding nominally undoped region are comparable to the highest conductive spots found on the doped ceramics ($N \approx 10^{20}$ cm^{-3} and $\mu \approx 5.5$ cm^2 V^{-1}s^{-1}).
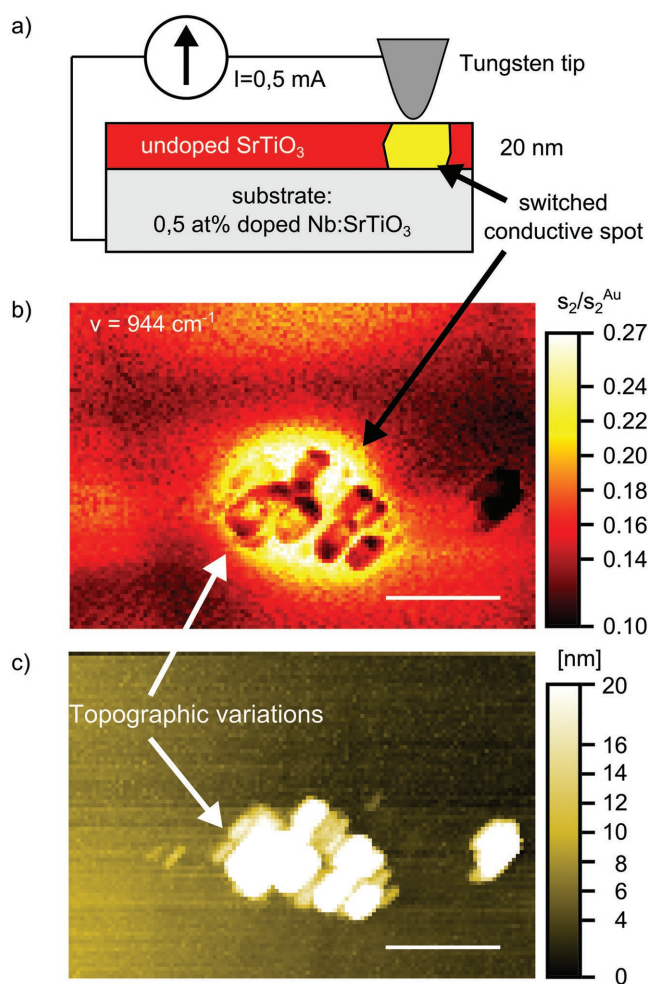

Figure 7. s-SNOM imaging of a locally switched spot in an undoped $SrTiO_3$ thin film. a) Sketch of the switching setup. b) Near-field optical amplitude image s_2/s_2^{Au} of the locally switched conductive spot at $v = 944$ cm^{-1}. c) Corresponding topography image. Additional features, which were created/deposited during the switching are marked by white arrows. Scale bar: 500 nm.

The dark spots in the switched region are correlated with topographic variations, as can be seen in the corresponding topography image in Figure 7c. They might stem from remainings of the point probe or result from the formation of an insulating SrO region during the switching.[66] Interestingly, also the surrounding unswitched region showed variations in the near-field amplitude signal similar to the inhomogeneities observed before in Nb- and La-doped $SrTiO_3$ single crystals by confocal Raman microscopy and fluorescence lifetime imaging.[17,18] The origin of those variations is still under debate as recent studies on Nb-doped single crystals did not find any evidence for a clustering of the dopant atoms.[67] Considering the plethora of open questions about the interplay of defects and charge carriers in $SrTiO_3$, our proof-of-principle promotes the application of s-SNOM for non-destructive defect and charge carrier mapping in ReRAM devices, 2DEGs and many other emerging phenomena and functionalities. Even an in operando 3D analysis of layered structures[68,37] is feasible as the penetration

depth of the signal can be tuned,[69] which allows in principle for nanotomography[70] below graphene top electrodes.[71]

8. Conclusion

In summary, we analyzed the influence of free charge carriers on the infrared near-field phonon resonance in La-doped $SrTiO_3$ ceramics. Using monochromatic near-field imaging, we could show that the infrared response is strongly varying on the nm scale. Mosaically shaped variations in the near-field optical amplitude images were identified as grain boundaries by EBSD. A quantitative analysis of the near-field optical amplitude spectra from $v = 580$ to 1500 cm^{-1} revealed local variations of the carrier density N by a factor of 4 and the high-frequency constant ε_∞ from 6.8 to 8.8. In contrast to spatially unresolved FTIR reflectivity spectra of the whole ceramic, the near-field spectra reveal a relatively high mobility $\mu \approx 5.5$ cm^2 V^{-1}s^{-1} of the charge carriers at grain boundaries and circular spots. In accordance with this interpretation, we were able to identify conducting regions at a locally switched conductive spot in a nominally undoped thin film of $SrTiO_3$. In conclusion, we set the basis for the application of s-SNOM for future subsurface carrier and defect profiling in ReRAM processes and other phenomena which alter the electronic properties in complex oxides on the nm scale, such as the formation of 2DEG. Fundamentally, the investigated coupling of the phonon- and free charge carrier near-field resonances is not limited to metal oxides, but can be found in many technologically relevant semiconductors as for example GaN and SiC. Apart from material characterization, the coupling was very recently exploited to enable actively tunable nanophotonic devices by tuning surface phonon polariton resonances.[40] Hence, we also envision the application of the non-volatile local redox-based switching in transition metal oxides as a building platform for 2D computable nanophotonic metasurfaces.[72]

9. Experimental Section

Ceramic Preparation: La-doped $SrTiO_3$ ceramics ($Sr_{1-x}La_xTiO_3$) were prepared by the conventional mixed-oxide technique, starting from $SrCO_3$ (Sigma–Aldrich, 99.9+%), fine-grained TiO_2 (Sigma–Aldrich, 99.9+%, < 5 µm), and $La(NO_3)_3$ x 6 H_2O (Sigma–Aldrich, 99.999 %). At first, appropriate amounts of $SrCO_3$ and TiO_2 were thoroughly mixed in a polyethylene-lined ball-mill using zirconia milling balls (diameter 2 and 3 mm) and 2-Propanol as the milling medium. The La dopant was added to the dried powder mixture by mixing in a $La(NO_3)_3$ x 6 H_2O solution in distilled water to form a viscous slurry. After drying, the mixture was calcined at 1150 °C for 16 h in air, yielding a single phase material (within the limit of detection) as analyzed by X-ray diffraction. The calcined material was then finely ground by ball-milling to a size < 1 µm. From this powder, cylindrical pellets (≈20 mm in diameter and ≈7 mm in height) were formed by cold isostatic pressing at 830 MPa. Before pressing, the powder was granulated by adding a liquid organic binder (Optapix PAF 35, Zschimmer and Schwarz, 3 wt% addition) in order to enhance the fracture strength of the pressed pellet. The binder was completely burnt off before sintering by firing at 600 °C for 12 h in air. Sintering of the samples was performed in a tube furnace at 1375 °C for 8 h under the flow of a dry 96% Ar 4% H_2 gas mixture, resulting in fine grained $Sr_{1-x}La_xTiO_3$ ceramics with densities around 99 % of the theoretical value. Specimens for the measurements were prepared by

cutting the sintered pellets into platelets and polishing selected facets to optical quality using standard procedures.

In order to normalize the near-field spectra and to serve as alignment markers for the EBSD characterization a matrix of gold patches was deposited on the ceramic. The 45 nm thick patches were created by optical lithography and the gold was deposited using a thermal evaporator.

Locally Switched Sample: Single-crystalline, nominally undoped $SrTiO_3$ thin films of 20 nm thickness were fabricated via pulsed laser deposition on 0.5 wt% Nb:$SrTiO_3$ substrates (CrysTec GmbH, Germany). The single-crystalline $SrTiO_3$ target was ablated by a KrF excimer laser ($\lambda = 248$ nm) with a repetition rate of 5 Hz and a spot size of 2 mm^2 at a target-to-substrate distance of 44 mm. The laser fluence was 1.45 J cm^{-2}. The sample was grown in an oxygen atmosphere of 0.1 mbar at a substrate temperature of 800 °C and the growth was monitored using reflection high-energy electron diffraction. For the forming of a conductive filament, voltages were applied to a tungsten whisker point probe with a nominal tip diameter of less than 1 µm in direct contact with the $SrTiO_3$ surface, while the Nb:$SrTiO_3$ substrate served as an electrically grounded bottom electrode, which was contacted through Al wire bonding. An I–V sweep was applied with a Keithley 2611A SourceMeter. At a voltage of approximately 5 V, the initially high resistance decreased suddenly and the current limit of 0.5 mA was reached.

Infrared Far-Field Characterization: The infrared far-field reflectivity spectrum of the $Sr_{0.997}La_{0.003}TiO_3$ ceramic was obtained using a commercial FTIR from Bruker ('Vertex 70') under an angle of incidence of approximately $\theta = 13$ °. The final spectrum is averaged over 512 single scans, which were recorded using a DLaTGS detector in the range from $v = 350$ to 8000 cm^{-1}at a spectral resolution of $v = 4$ cm^{-1}. The reflectivity spectrum is normalized to the reflectivity spectrum of a flat gold mirror.

Infrared Near-Field Imaging: A commercially available s-SNOM system (Neaspec) was used with a pseudoheterodyne module to obtain in parallel the optical amplitude and topography signal. A mercury cadmium telluride detector (InfraRed associates) is used to detect the optical signals. All optical amplitude signals in this publication are demodulated at the second harmonic of the tip oscillation frequency $\omega \approx 250$ kHz to suppress far-field background contributions. As scattering tip commercially available platinum–iridium-coated silicon tips with a radius of curvature $r < 25$ nm were employed (ArrowNCPt, NanoAndMore). For all near-field investigations in this publication, the tapping amplitude was adjusted to approximately 40 nm. To identify electronic inhomogeneities using monochromatic imaging at $v = 944$ cm^{-1}, a continuous wave CO_2 laser from Edinburgh Instruments with a high signal-to-noise ratio was used (acquisition time: for example, the image in Figure 2a) was taken over a period of approximately 30 min (≈0.9 min µm^{-2}). Furthermore, near-field amplitude spectra were collected in the range from $v = 871$ to 1510 cm^{-1} by sequentially imaging the same region at different wavelengths of illumination of a monochromatic light source. Here, a continuous wave tunable quantum cascade laser (MIRCAT) from Daylight solutions was used.

Infrared Near-Field Spectroscopy: Near-field optical amplitude spectra at a single tip position were acquired by using a commercially available nano-FTIR module for the s-SNOM system (Neaspec) in combination with a home-built tunable broad-band laser by the Fraunhofer Institute for Lasertechnology (ILT).[32,52] The laser system consists of a commercially available picosecond laser and two subsequent non-linear converter stages to cover the mid-infrared range. The first stage is an optical parametric generator (OPG), which shifts the wavelength of the pump laser from 1 µm to tunable output between 1.7 and 2.02 µm (signal) and 2.25 and 2.8 µm (idler). In the subsequent difference frequency generation (DFG) unit signal and idler output of the OPG are mixed to obtain longer wavelengths. By means of a CdSe crystal, the peak wavelength of the DFG output is continuously tunable from 12.8 to 16 µm with bandwidths of some tens to more than hundred wavenumbers. The average output power is 1 mW. The nano-FTIR module consists of an interferometric setup. One half of the broad band intensity is guided by a beamsplitter to the scattering tip, while the

**ADVANCED
SCIENCE NEWS**

www.advancedsciencenews.com

**ADVANCED
FUNCTIONAL
MATERIALS**

www.afm-journal.de

other half of the intensity is directed to a movable mirror. The signals from both arms are recombined and detected in a mercury cadmium telluride detector. Interferograms of both signals are recorded by demodulating the signal at the second harmonic of the tip oscillation frequency $\omega \approx 250$ kHz and linearly moving the reference mirror for $d = 750$ µm. After a Fourier transformation, a local near-field amplitude spectrum $s_2(v)$ with a spectral resolution of $\Delta v = 6.7$ cm^{-1} is obtained, which is normalized to a reference spectrum $s_2^{Au}(v)$ on an adjacent 45 nm thick gold film. To yield a sufficient signal-to-noise ratio, each spectrum is averaged over 10 single spectra. To cover the full spectral range of the $SrTiO_3$ near-field phonon resonance, amplitude spectra are recorded sequentially for three different central wavelengths of the broad-band laser system. In between the drift of the tip is corrected by monochromatic imaging of the region of interest and subsequent correction of the tip position. Finally, all three spectra are combined into one single spectrum. The spectrum in the overlapping region is calculated from a weighted average based on the relative intensities in the gold reference spectra $s_2^{Au}(v)$.

Electron Microscopy to Image Grain Boundaries: EBSD measurements of selected analyzed areas were performed using a Hikari camera by Ametek-EDAX attached to a JSM-7000F field emission scanning electron microscope by JEOL. The measurement areas were scanned with a step size of 50 nm using 20 keV electrons and a probe current of approximately 30 nA. The EBSD patterns were collected and indexed with the software implemented $SrTiO_3$ database phase using OIM Data Collection, and finally evaluated with respect to the misorientation angles using OIM analysis, both in V7.3 by Ametek-EDAX.

Supporting Information

Supporting Information is available from the Wiley Online Library or from the author.

Conflict of Interest

The authors declare no conflict of interest.

[1] H. Wu, X. H. Wang, B. Gao, N. Deng, Z. Lu, B. Haukness, G. Bronner, H. Qian, *Proc. IEEE* **2017**, *105*, 1770.
[2] H. Takagi, H. Y. Hwang, *Science* **2010**, *327*, 1601.
[3] J. Mannhart, D. G. Schlom, *Science* **2010**, *327*, 1607.
[4] A. Ohtomo, H. Y. Hwang, *Nature* **2004**, *427*, 423.
[5] A. F. Santander-Syro, O. Copie, T. Kondo, F. Fortuna, S. Pailhès, R. Weht, X. G. Qiu, F. Bertran, A. Nicolaou, A. Taleb-Ibrahimi, P. Le Fèvre, G. Herranz, M. Bibes, N. Reyren, Y. Apertet, P. Lecoeur, A. Barthélémy, M. J. Rozenberg, *Nature* **2011**, *469*, 189.
[6] R. Jany, C. Richter, C. Woltmann, G. Pfanzelt, B. Förg, M. Rommel, T. Reindl, U. Waizmann, J. Weis, J. A. Mundy, D. A. Muller, H. Boschker, J. Mannhart, *Adv. Mater. Interfaces* **2013**, *1*, 1300031.
[7] C. Woltmann, T. Harada, H. Boschker, V. Srot, P. A. van Aken, H. Klauk, J. Mannhart, *Phys. Rev. Appl.* **2015**, *4*, 064003.
[8] J. Verbeeck, S. Bals, A. N. Kravtsova, D. Lamoen, M. Luysberg, M. Huijben, G. Rijnders, A. Brinkman, H. Hilgenkamp, D. H. A. Blank, G. Van Tendeloo, *Phys. Rev. B.* **2010**, *81*, 14.
[9] M. Lee, R. Arras, B. Warot-Fonrose, T. Hungria, M. Lippmaa, H. Daimon, M. J. Casanove, *Phys. Chem. Chem. Phys.* **2017**, *19*, 28676.
[10] R. Waser, R. Dittmann, G. Staikov, K. Szot, *Adv. Mater.* **2009**, *21*, 2632.
[11] D. Ielmini, R. Waser, H. Akinaga, H. Shima, H. S. P. Wong, J. J. Yang, S. Yu, in *Resistive Switching* (Eds: D. Ielmini, R. Waser), Wiley-VCH, Weinheim, Germany **2016**, pp. 1–30.
[12] K. Szot, W. Speier, G. Bihlmayer, R. Waser, *Nat. Mater.* **2006**, *5*, 312.
[13] C. Baeumer, R. Valenta, C. Schmitz, A. Locatelli, T. O. Menteş, S. P. Rogers, A. Sala, N. Raab, S. Nemsak, M. Shim, C. M. Schneider, S. Menzel, R. Waser, R. Dittmann, *ACS Nano* **2017**, *11*, 6921.
[14] H. Du, C.-L. Jia, A. Koehl, J. Barthel, R. Dittmann, R. Waser, J. Mayer, *Chem. Mater.* **2017**, *29*, 3164.
[15] C. Baeumer, C. Schmitz, A. Marchewka, D. N. Mueller, R. Valenta, J. Hackl, N. Raab, S. P. Rogers, M. I. Khan, S. Nemsak, M. Shim, S. Menzel, C. M. Schneider, R. Waser, R. Dittmann, *Nat. Commun.* **2016**, *7*, 12398.
[16] S. von Alfthan, N. A. Benedek, L. Chen, A. Chua, D. Cockayne, K. J. Dudeck, C. Elsässer, M. W. Finnis, C. T. Koch, B. Rahmati, M. Rühle, S.-J. Shih, A. P. Sutton, *Annu. Rev. Mater. Res.* **2010**, *40*, 557.
[17] C. Rodenbücher, T. Gensch, W. Speier, U. Breuer, M. Pilch, H. Hardtdegen, M. Mikulics, E. Zych, R. Waser, K. Szot, *Appl. Phys. Lett.* **2013**, *103*, 162904.
[18] C. Rodenbücher, A. Jauß, V. Havel, R. Waser, K. Szot, *Phys. Status Solidi RRL* **2014**, *08*, 781.
[19] W. G. Spitzer, R. C. Miller, D. A. Kleinman, L. E. Howarth, *Phys. Rev.* **1962**, *126*, 1710.
[20] A. Rubano, L. Braun, M. Wolf, T. Kampfrath, *Appl. Phys. Lett.* **2012**, *101*, 081103.
[21] D. A. Crandles, B. Nicholas, C. Dreher, C. C. Homes, A. W. McConnell, B. P. Clayman, W. H. Gong, J. E. Greedan, *Phys. Rev. B* **1999**, *59*, 12842.
[22] F. Gervais, J.-L. Servoin, A. Baratoff, J. G. Bednorz, G. Binnig, *Phys. Rev. B* **1993**, *47*, 8187.
[23] J. L. Servoin, Y. Luspin, F. Gervais, *Phys. Rev. B* **1980**, *22*, 5501.
[24] F. Keilmann, R. Hillenbrand, *Phil. Trans. R. Soc.* **2004**, *362*, 787.
[25] F. Huth, M. Schnell, J. Wittborn, N. Ocelic, R. Hillenbrand, *Nat. Mater.* **2011**, *10*, 352.
[26] F. Huth, A. Govyadinov, S. Amarie, W. Nuansing, F. Keilmann, R. Hillenbrand, *Nano Lett.* **2012**, *12*, 3973.
[27] I. Amenabar, S. Poly, M. Goikoetxea, W. Nuansing, P. Lasch, R. Hillenbrand, *Nat. Commun.* **2017**, *8*, 14402.
[28] R. Hillenbrand, T. Taubner, F. Keilmann, *Nature* **2002**, *418*, 159.
[29] B. Knoll, F. Keilmann, *Appl. Phys. Lett.* **2000**, *77*, 3980.
[30] A. J. Huber, D. Kazantsev, F. Keilmann, J. Wittborn, R. Hillenbrand, *Adv. Mater.* **2007**, *19*, 2209.
[31] A. Cvitkovic, N. Ocelic, R. Hillenbrand, *Opt. Express* **2007**, *15*, 8550.
[32] S. Bensmann, F. Gaußmann, M. Lewin, J. Wüppen, S. Nyga, C. Janzen, B. Jungbluth, T. Taubner, *Opt. Express* **2014**, *22*, 22369.

[33] A. M. Gigler, A. J. Huber, M. Bauer, A. Ziegler, R. Hillenbrand, R. W. Stark, *Opt. Express* **2009**, *17*, 22351.

[34] J. M. Stiegler, A. J. Huber, S. L. Diedenhofen, J. Gómez Rivas, R. E. Algra, E. P. A. M. Bakkers, R. Hillenbrand, *Nano Lett.* **2010**, *10*, 1387.

[35] J. M. Stiegler, R. Tena-Zaera, O. Idigoras, A. Chuvilin, R. Hillenbrand, *Nat. Commun.* **2012**, *3*, 1131.

[36] B. Hauer, T. Saltzmann, U. Simon, T. Taubner, *Nano Lett.* **2015**, *15*, 2787.

[37] L. Jung, D. S. Boyuk, A. T. Mohabir, M. A. Filler, T. Taubner, unpublished.

[38] S. Ohta, T. Nomura, H. Ohta, K. Koumoto, *J. Appl. Phys.* **2005**, *97*, 034106.

[39] A. S. Barker, in *Optical Properties and Electronic Structure of Metals and Alloys* (Ed: F. Abeles), North-Holland Publishing Company, Amsterdam, Netherlands **1966**, pp. 452–468.

[40] A. D. Dunkelberger, C. T. Ellis, D. C. Ratchford, A. J. Giles, M. Kim, C. S. Kim, B. T. Spann, I. Vurgaftman, J. G. Tischler, J. P. Long, O. J. Glembocki, J. C. Owrutsky, J. D. Caldwell, *Nat. Photonics* **2018**, *12*, 50.

[41] A. Huber, N. Ocelic, T. Taubner, R. Hillenbrand, *Nano Lett.* **2006**, *6*, 774.

[42] D. J. Lahneman, T. J. Huffman, P. Xu, S. L. Wang, T. Grogan, M. M. Qazilbash, *Opt. Express* **2017**, *25*, 20421.

[43] L. Cheng, D.-L. Wang, S.-Y. Dai, Y.-D. Yan, X.-D. Fan, L.-M. Wei, C.-G. Zeng, *J. Infrared Millim. Waves (Chin. Opt. Soc.)* **2017**, *36*, 534.

[44] R. Moos, K. H. Härdtl, *J. Appl. Phys.* **1996**, *80*, 393.

[45] J. T. Devreese, S. N. Klimin, J. L. M. van Mechelen, D. van der Marel, *Phys. Rev. B* **2010**, *81*, 125119.

[46] P. Hermann, A. Hoehl, G. Ulrich, C. Fleischmann, A. Hermelink, B. Kästner, P. Patoka, A. Hornemann, B. Beckhoff, E. Rühl, G. Ulm, *Opt. Express* **2014**, *22*, 17948.

[47] H. A. Bechtel, E. A. Muller, R. L. Olmon, M. C. Martin, M. B. Raschke, *Proc. Natl. Acad. Sci. USA* **2014**, *111*, 7191.

[48] S. Schneider, J. Seidel, S. Grafström, L. M. Eng, S. Winnerl, D. Stehr, M. Helm, *Appl. Phys. Lett.* **2007**, *90*, 143101.

[49] M. Ishikawa, M. Katsura, S. Nakashima, Y. Ikemoto, H. Okamura, *Opt. Express* **2012**, *20*, 11064.

[50] S. Amarie, F. Keilmann, *Phys. Rev. B* **2011**, *83*, 045404.

[51] S. Amarie, P. Zaslansky, Y. Kajihara, E. Griesshaber, W. W. Schmahl, F. Keilmann, *Beilstein J. Nanotechnol.* **2012**, *3*, 312.

[52] J. Wueppen, B. Jungbluth, T. Taubner, P. Loosen, *Ultrafast tunable mid IR source*, in 36th International Conference on Infrared, Millimeter, and Terahertz Waves (IRMMW-Thz), Vol. *1*, IEEE, Houston **2011**, pp. 2–7.

[53] M. D. Rossell, Q. M. Ramasse, S. D. Findlay, F. Rechberger, R. Erni, M. Niederberger, *ACS Nano* **2012**, *6*, 7077.

[54] R. Waser, R. Hagenbeck, *Acta Mater.* **2000**, *48*, 797.

[55] R. A. De Souza, F. Gunkel, S. Hoffmann-Eifert, R. Dittmann, *Phys. Rev. B* **2014**, *89*, 241401.

[56] S. Rodewald, J. Fleig, J. Maier, *J. Am. Ceram. Soc.* **2001**, *84*, 521.

[57] R. A. De Souza, *Phys. Chem. Chem. Phys.* **2009**, *11*, 9939.

[58] R. Meyer, A. F. Zurhelle, R. A. De Souza, R. Waser, F. Gunkel, *Phys. Rev. B* **2016**, *94*, 115408

[59] A. Ohtomo, H. Y. Hwang, *Appl. Phys. Lett.* **2004**, *84*, 1716.

[60] M. Andrä, F. Dvořák, M. Vorokhta, S. Nemsak, V. Matolín, C. M. Schneider, R. Dittmann, F. Gunkel, D. N. Mueller, R. Waser, *APL Mater.* **2017**, *5*, 056106.

[61] F. Gunkel, P. Brinks, S. Hoffmann-Eifert, R. Dittmann, M. Huijben, J. E. Kleibeuker, G. Koster, G. Rijnders, R. Waser, *Appl. Phys. Lett.* **2012**, *100*, 052103.

[62] R. Muenstermann, T. Menke, R. Dittmann, S. Mi, C.-L. Jia, D. Park, J. Mayer, *J. Appl. Phys.* **2010**, *108*, 124504.

[63] E. T. Ritchie, D. J. Hill, T. M. Mastin, P. C. Deguzman, J. F. Cahoon, J. M. Atkin, *Nano Lett.* **2017**, *17*, 6591.

[64] P. Calvani, M. Capizzi, F. Donato, S. Lupi, P. Maselli, D. Peschiaroli, *Phys. Rev. B* **1993**, *47*, 8917.

[65] M. Buckwell, L. Montesi, A. Mehonic, O. Reza, L. Garnett, M. Munde, S. Hudziak, A. J. Kenyon, *Phys. Status Solidi C* **2015**, *12*, 211.

[66] C. Baeumer, N. Raab, T. Menke, C. Schmitz, R. Rosezin, P. Müller, M. Andrä, V. Feyer, R. Bruchhaus, F. Gunkel, C. M. Schneider, R. Waser, R. Dittmann, *Nanoscale* **2016**, *8*, 13967.

[67] C. Rodenbücher, M. Luysberg, A. Schwedt, V. Havel, F. Gunkel, J. Mayer, R. Waser, *Sci. Rep.* **2016**, *6*, 32250.

[68] M. Lewin, B. Hauer, M. Bornhöfft, L. Jung, J. Benke, A. K. U. Michel, J. Mayer, M. Wuttig, T. Taubner, *Appl. Phys. Lett.* **2015**, *107*, 151902.

[69] R. Krutokhvostov, A. A. Govyadinov, J. M. Stiegler, F. Huth, A. Chuvilin, P. S. Carney, R. Hillenbrand, *Opt. Express* **2012**, *20*, 593.

[70] A. A. Govyadinov, S. Mastel, F. Golmar, A. Chuvilin, P. S. Carney, R. Hillenbrand, *ACS Nano* **2014**, *8*, 6911.

[71] P. Li, T. Wang, H. Böckmann, T. Taubner, *Nano Lett.* **2014**, *14*, 4400.

[72] P. Li, X. Yang, T. W. W. Maß, J. Hanss, M. Lewin, A.-K. U. Michel, M. Wuttig, T. Taubner, *Nat. Mater.* **2016**, *15*, 870.

1802834 (11 of 11)